Journal of Materials Chemistry A

ROYAL SOCIETY OF CHEMISTRY

PAPER

View Article Online
View Journal | View Issue

Cite this: J. Mater. Chem. A, 2024, 12, 10764

Foldable chromium vanadate cathodes for high-performance aqueous zinc ion batteries†

Peiqi Shi,‡[ab] Meng Huang,‡[b] Lianmeng Cui,[a] Bomian Zhang,[ab] Lei Zhang,[ab] Qinyou An *[ab] and Liqiang Mai*[ab]

Received 28th December 2023
Accepted 26th March 2024

DOI: 10.1039/d3ta08078a

rsc.li/materials-a

Aqueous zinc ion batteries (AZIBs), featuring intrinsic high safety, low cost, and environmental benignity, are one promising candidate for scalable energy storage. Vanadium-based materials show great potential as cathodes for AZIBs. However, either low electronic conductivity or structural collapse limits their practical applications. Herein, we report a novel $CrV_{2.7}O_{4.36}\cdot 2.85H_2O$ (CVO) nanoflower, carbon nanotube (CNT), and reduced graphene oxide (rGO) composite (CVO/CNT-rGO) cathode. The rGO and CNT framework can improve electronic conductivity and inhibit structural collapse, and the introduced Cr^{3+} can also stabilize the lattice structure. As a result, the CVO/CNT-rGO exhibits a high capacity (397 mA h g^{-1} at 0.2 A g^{-1}), high rate performance (252 mA h g^{-1} at 5 A g^{-1}), and long cyclability (87% capacity retention after 1000 cycles). It also shows a Zn^{2+}/H^+ insertion/extraction mechanism. Additionally, the high conductivity and flexibility of CVO/CNT-rGO endow the CVO/CNT-rGO//Zn pouch cell with satisfactory cyclability at various folding states.

1. Introduction

In today's era of limited fossil energy reserves and low-carbon environmental protection, large-scale green energy harvest is of great importance. Owing to the long cycling performance and high energy density, lithium-ion batteries (LIBs) are widely used in electric vehicles and portable equipment.[1–5] Nevertheless, scarce lithium resources and flammable organic electrolytes limit further development.[6,7] In contrast, compared to other batteries, aqueous zinc ion batteries (AZIBs) show great potential due to their high safety, low cost, and environmental benignity. In addition, the zinc metal anode has a high specific capacity (820 mA h g^{-1}, 5855 mA h cm^{-3}), relatively low redox potential (−0.76 V *vs.* SHE), and excellent stability in aqueous solution.[8] However, the cathodes for AZIBs suffer from many problems, such as side reactions, low energy density, and dissolution, all of which hinder the development of AZIBs. Therefore, it is essential to design a cathode material with high cyclability and capacity for AZIBs.[9,10] In addition, the growing demand for flexible and foldable devices propels the advancement of wearable electric devices. Maintaining the electrochemical performances of electronic equipment in a flexible or foldable state is still a significant challenge.[11]

Nowadays, promising cathode materials for AZIBs include vanadium-based materials,[12,13] manganese-based materials,[14,15] Prussian blue analogs,[16,17] and other materials.[18] Among them, vanadium-based materials not only have a large layer spacing but also have various valence states. However, the low electronic conductivity, vanadium dissolution, and slow diffusion kinetics still limit the development of vanadium-based materials.[19] Many attempts have been made to solve the above problems, and one basic strategy is to introduce water molecules and/or pre-intercalated ions, including alkali metal ions (Li^+, Na^+, and K^+), alkaline earth metal ions (Ca^{2+} and Mg^{2+}), rare earth metal ions (La^{3+}), and other species (Al^{3+}).[20–26] For example, $MnV_{12}O_{31}\cdot 10H_2O$ (MNVO) nanoflowers obtained *via* a one-step hydrothermal method to introduce Mn^{2+} into the vanadium–oxygen skeleton have a high capacity of 433 mA h g^{-1} at 0.1 A g^{-1}, of which 81.5% is retained after 5000 cycles.[27] Chromium (Cr) is a transition metal element with multivalent states, and it also has great potential as a functional dopant ion. Furthermore, Cr–O (461 kJ mol^{-1})[28] has a stronger bond energy than those of reported Mg–O (358 kJ mol^{-1}), Na–O (270 kJ mol^{-1}),[29] Mn–O (402 kJ mol^{-1}), and Ni–O (382 kJ mol^{-1}),[30] which is favorable for stabilizing the lattice framework. To improve the electronic conductivity and suppress structural collapse, decorating with carbon materials can be applied.[31] In terms of flexible devices, conductive carbon materials and carbon nanotube paper/fibers, for instance, are commonly used as the matrix.[32–35] Therefore, interconnecting

[a]State Key Laboratory of Advanced Technology for Materials Synthesis and Processing, Wuhan University of Technology, Wuhan, 430070, P.R. China. E-mail: anqinyou86@whut.edu.cn; mlq518@whut.edu.cn

[b]The Sanya Science and Education Innovation Park, Wuhan University of Technology, Sanya, 572000, P.R. China

† Electronic supplementary information (ESI) available. See DOI: https://doi.org/10.1039/d3ta08078a

‡ These authors contributed equally to this work.

carbon materials with active materials is also a reasonable approach for the design of flexible AZIBs.

In this work, we design a $CrV_{2.7}O_{4.36}\cdot 2.85H_2O$ (CVO) nanoflower, carbon nanotube (CNT) and reduced graphene oxide (rGO) composite (CVO/CNT-rGO) as a cathode for AZIBs by a one-pot hydrothermal method. The Cr^{3+} can stabilize the structure through the strong Cr–O bond, and rGO and CNTs can enhance the electronic conductivity. In addition, the interconnected CNT and rGO framework can suppress the volume expansion/shrinkage of CVO upon dis-/charge, and the increased specific surface area improves Zn^{2+} diffusion kinetics. As a result, the CVO/CNT-rGO exhibits a high capacity (397 mA h g^{-1} at 0.2 A g^{-1}), high rate capability (252 mA h g^{-1} at 5 A g^{-1}), and long-term cyclability (87% capacity retention after 1000 cycles). *Ex situ* XRD and XPS investigations demonstrate the high reversibility of CVO/CNT-rGO in the Zn^{2+} de-/intercalation process. Furthermore, the assembled CVO/CNT-rGO//Zn pouch cells have stable electrochemical performance at different folding states. This work could provide valuable insights for designing stable cathodes and the applications of foldable electronics for AZIBs.

2. Results and discussion

2.1 Morphological and compositional characterization

Fig. 1a describes the synthesis process of CVO/CNT-rGO, including a simple one-step hydrothermal process and subsequent freeze-drying. Generally, rGO is obtained by hydrothermal reduction of GO, and then CNTs are also introduced to enhance its electrical conductivity with the hydrothermal reaction.[36] The XRD patterns of the three samples show several weak diffraction peaks that closely match the (001), (002), (003), (110), (005), (006), and (40-5) crystal planes of the monoclinic crystal structure of $H_{11}Al_2V_6O_{23.2}$ (PDF No. 49-0693) (Fig. 1b). Thus, the addition of CNTs and/or rGO has little effect on the crystal structure of CVO. TEM images show that CVO has a nanoflower morphology (Fig. 1c and d). EDS spectra indicate the elements (Cr, V, O) are uniformly distributed in the CVO nanoflowers (Fig. S1†). The CVO/CNT is formed by the attachment of CVO nanoflowers to CNTs (Fig. S2†). In addition, CVO/CNT-rGO still has the nanoflower structure (Fig. 1e and f). The HRTEM images of CVO/CNT-rGO show well-defined lattice fringes of 3.46 Å, corresponding to the (110) plane (Fig. 1g). The EDS spectrum shows that the element C is uniformly distributed (Fig. S3†). The Raman spectra of CVO and CVO/CNT-rGO are relatively similar, except for the peaks at 1350 and 1596 cm^{-1} for CVO/CNT-rGO (Fig. 1h). The bending vibration peak of the –O–V–O–V– chains is located at 156 cm^{-1}, and the peaks of the V=O bending vibrations are located at 267 cm^{-1} and 949 cm^{-1}. The peaks at 519 and 701 cm^{-1} are associated with the V–O_t (O_t denotes a terminal oxygen atom) vibration.[37] The D-band and G-band at 1350 and 1596 cm^{-1} are attributed to the disordered vibrations of the C atom in the graphene and sp^2 bond, respectively.[38] In the Fourier transform infrared (FTIR) spectra, the peaks at 524 cm^{-1} and 727 cm^{-1} derive from V–O–V stretching, and that at 1008 cm^{-1} represents V=O stretching of [VO_5] square pyramids (Fig. S4†). Besides, the vibration peaks of H_2O molecules are located at 1613 and 3420 cm^{-1}.[39]

The XPS result shows that CVO/CNT-rGO mainly contains Cr, V, O, and C elements (Fig. S5a†). The peaks situated at 577.8 and 587.6 eV are associated with Cr^{3+} $2p_{3/2}$ and Cr^{3+} $2p_{1/2}$, respectively (Fig. 1i).[40] In the V 2p spectrum (Fig. 1j), the peaks at 516.2 and 517.6 eV derive from V $2p_{3/2}$ of V^{4+} and V^{5+}, and those at 523.8 and 525.2 eV correspond to V $2p_{1/2}$ of V^{4+} and V^{5+}, respectively.[41] The peaks at 530.3, 531.4, and 533.4 eV come from the bonding of V–O, O–H, and H_2O, respectively (Fig. S5b†).[27] The C–C, C–O, and C=O peaks situate at 284.8, 285.4, and 288.2 eV, respectively (Fig. S5c†). Inductively coupled plasma (ICP) measurements indicate that the Cr/V molar ratio is 1/2.7 in the CVO (Table S1†). The organic element analysis (C/H/O/N/S) test (Table S2†) shows the total molar ratio of H and O in CVO is approximately 1/1.26. In Fig. S6,† the thermogravimetric (TG) curves of two samples were tested under an air atmosphere with an increase rate of 10 °C min^{-1}. The results showed that the mass reduction of the CVO and CVO/CNT-rGO between 100 °C and 360 °C is 11.29% and 11.31%, respectively, which corresponds to 2.85 H_2O molecules per CVO molecule. Therefore, the formula of the CVO is determined to be $CrV_{2.7}O_{4.36}\cdot 2.85H_2O$ (Table S3†). As shown in Fig. S7,† CVO and CVO/CNT-rGO show H3-type hysteresis loops, and thus they both show the presence of mesopores, distributing at 1.9–50 and 1.7–60 nm, respectively. The specific surface area of CVO and CVO/CNT-rGO is 46.18 and 57.90 m^2 g^{-1}, respectively. The larger value for CVO/CNT-rGO is attributed to the presence of CNTs and rGO, which can provide superior electrolyte access, more active sites, and a shorter Zn^{2+} diffusion path.[42] And the mesoporous structure could suppress the volume changes induced by Zn^{2+} intercalation.[43]

2.2 Electrochemical properties characterization

To investigate the electrochemical performance of the CVO/CNT-rGO cathode in AZIBs, a zinc plate, 4 M $Zn(CF_3SO_3)_2$, and glass fibers are used as the anode electrode, electrolyte, and separator, respectively. The CV curves of CVO, CVO/CNT, and CVO/CNT-rGO were obtained (Fig. 2a). It could be seen that the CVO electrode has the lowest current and the smallest area of the curve, and in contrast, CVO/CNT-rGO exhibits the strongest current and the largest area of the curve, and thus has the highest specific capacity. It is worth mentioning that the three samples have similar reaction processes, which is not affected by the addition of CNTs and/or rGO. The two pairs of peaks located at 1.02/0.9 and 0.75/0.6 V correspond to the redox peaks of V^{5+}/V^{4+} and V^{4+}/V^{3+}, respectively.[19] The initial discharge/charge specific capacities of CVO, CVO/CNT, and CVO/CNT-rGO are 252/260, 316/326, and 397/418 mA h g^{-1}, respectively (Fig. 2b) and the charge/discharge curves of CVO/CNT-rGO have the most smooth voltage plateaus. This means that there is a multistep intercalation/deintercalation process of Zn^{2+} in the CVO/CNT-rGO cathodes.[44] Fig. 2c shows that the CVO, CVO/CNT, and CVO/CNT-rGO provide an initial discharge capacity of 252.2, 315.3, and 397.3 mA h g^{-1} at 0.2 A g^{-1}. At the low

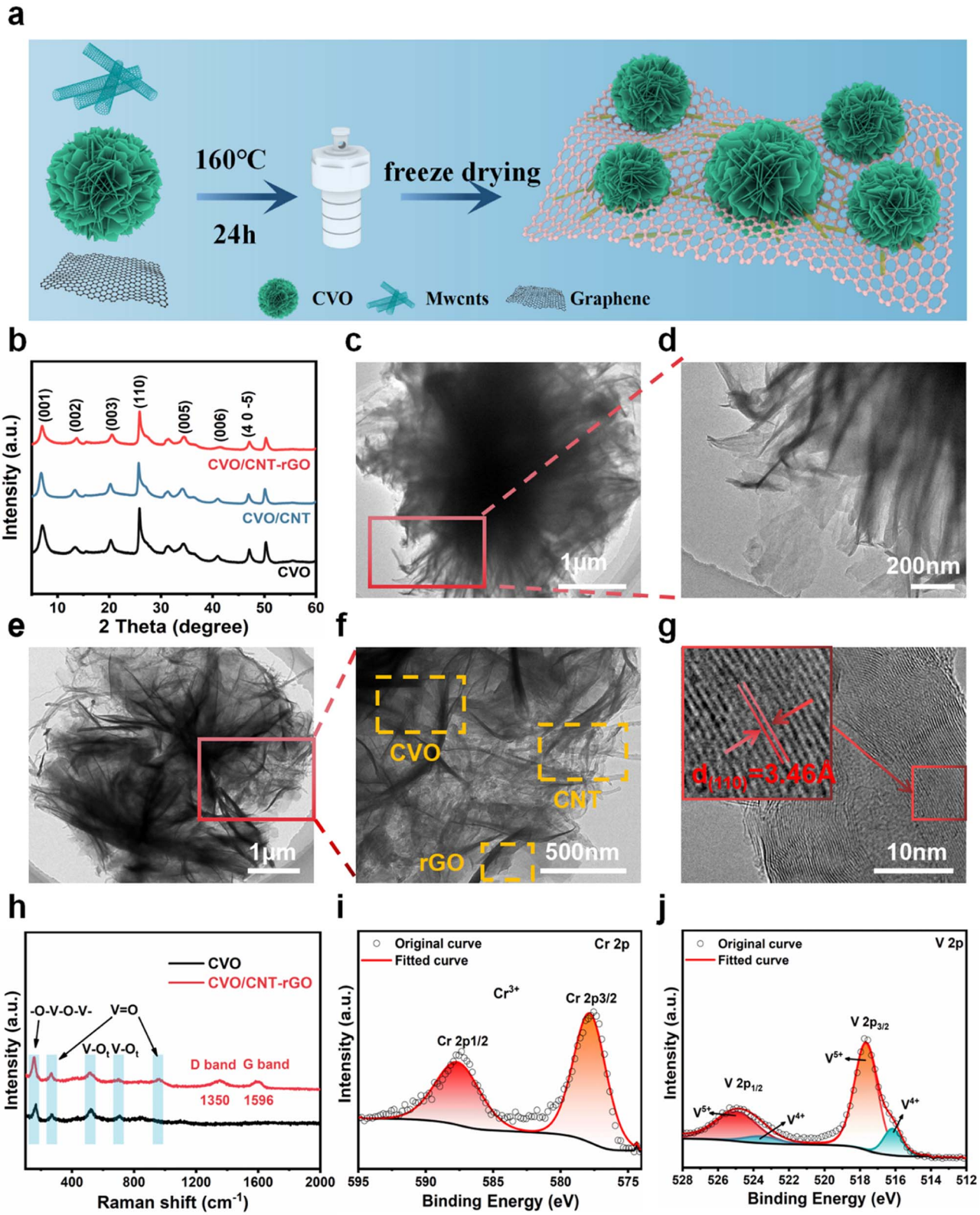

Fig. 1 (a) Synthesis schematic of the CVO/CNT-rGO. (b) XRD patterns. (c and d) TEM images of CVO. (e and f) TEM images of CVO/CNT-rGO. (g) HRTEM image of CVO/CNT-rGO. (h) Raman spectra of CVO and CVO/CNT-rGO. (i) XPS spectra of Cr 2p. (j) XPS spectra of V 2p.

current density of 0.01 A g^{-1}, CVO can also show a high discharge specific capacity of 389 mA h g^{-1}, which is close to that of CVO/CNT-rGO (397 mA h g^{-1} at 0.2 A g^{-1}). The addition of CNTs and rGO improves the electronic conductivity of CVO, stabilizes the structure and improves the discharge depth, so that CVO/CNT-rGO can release greater capacity at higher

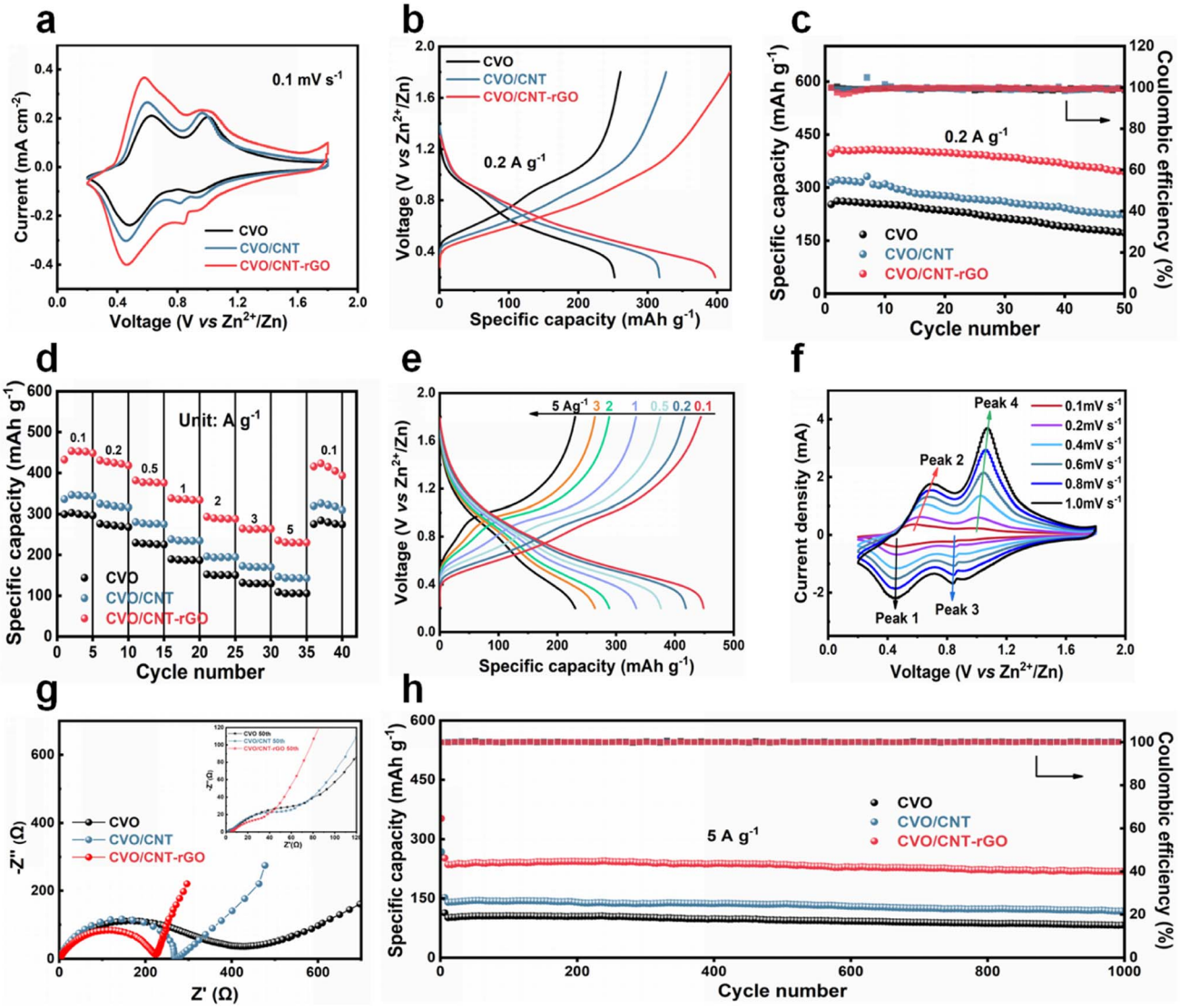

Fig. 2 (a) CV curves of the CVO, CVO/CNT, and CVO/CNT-rGO at 0.1 mV s^{-1}. (b) Galvanostatic charge–discharge curves of CVO, CVO/CNT, and CVO/CNT-rGO. (c) Cycling performance of CVO, CVO/CNT, and CVO/CNT-rGO at 0.2 A g^{-1}. (d) Rate performance of the CVO/CNT-rGO. (e) Corresponding charge–discharge curves at different current densities. (f) The CV curves of CVO/CNT-rGO at different scan rates. (g) EIS spectra of CVO, CVO@CNT, and CVO/CNT-rGO before and after 50 cycles at 0.2 A g^{-1}. (h) Cycling performance at 5 A g^{-1}.

current densities (Fig. S8†). The CVO/CNT-rGO has a larger improvement in the initial discharge process than the other two samples. After cycling 50 times, they show a capacity retention of 68%, 70%, and 87%, respectively. As the current density changes from 0.1 to 0.2, 0.5, 1.0, 2.0, 3.0, and 5.0 A g^{-1}, average discharge capacities of CVO/CNT-rGO are 448, 424, 377, 335, 289, 263, and 231 mA h g^{-1}, respectively (Fig. 2d). The average discharge capacity remains at 410 mA h g^{-1} when the current density returns to 0.1 A g^{-1}, demonstrating a high rate capability and cyclability. In addition, the discharge plateau of CVO/CNT-rGO at various current densities does not change significantly (Fig. 2e). After 1000 cycles, CVO/CNT-rGO still maintains the nanoflower structure (Fig. S9a and b, S10a†), but CVO has completely changed from the nanoflower structure to a broken granular structure (Fig. S9c and d, S10c†). The HRTEM image of CVO/CNT-rGO shows the lattice fringes of 3.42 Å, corresponding to the (110) plane (Fig. S10b†). In contrast, the CVO has transformed into an amorphous state (Fig. S10d†). These excellent electrochemical performances of CVO/CNT-rGO are probably attributed to the rGO and CNTs increasing the conductivity, and rGO suppressing the structural degradation of CVO nanoflowers and inhibiting vanadium dissolution. As is shown in Fig. S11,† CVO shows a more obvious dissolution than CVO/CNT-rGO after 100 cycles. Fig. 2f shows the CV curves at separated scan rates (0.1 to 1 mV s^{-1}). To further ascertain the electrochemical process in CVO/CNT-rGO, the correlations between peak current i and scan rate v are determined using the following equations.[45]

$$i = av^b \quad (1)$$

$$\log i = b \log v + \log a \quad (2)$$

$$i = k_1 v + k_2 v^{1/2} \quad (3)$$

A b-value of 1 reflects a capacitance-controlled process, and 0.5 indicates a diffusion-controlled process. The b-values of the four peaks are 0.738, 0.680, 0.865, and 1.189, respectively (Fig. S12a†). The results show that the whole electrochemical process is controlled by ion-diffusion and capacitive processes. In addition, the capacitive contribution proportion is determined by eqn (3).[46] Here, k_1v and $k_2v^{1/2}$ are the contributions of capacitance-controlled and diffusion-controlled parts, respectively. The percentages of diffusion control and capacitance contribution were calculated and are shown in Fig. S12b.† The capacitive contributions increase from 56% to 79% between the scan rates of 0.1 and 1 mV s^{-1} (Fig. S12c†), indicating that the capacitive process gradually becomes dominant. Fig. S12d† shows the GITT test of the CVO/CNT-rGO electrode which helps to investigate the Zn^{2+} diffusion kinetics.[47]

$$D^{\mathrm{GITT}} = \frac{4}{\pi\tau}\left(\frac{m_B V_M}{M_B S}\right)^2 \left(\frac{\Delta E_s}{\Delta E_\tau}\right)^2 \quad (4)$$

Eqn (4) is used to calculate the Zn^{2+} diffusion coefficients (D^{GITT}). The change of potential in the process of the constant current pulse is represented by ΔE_τ, and the open-circuit potential difference corresponds to the ΔE_s. The mass, molar mass, molar volume, relaxation time, and electrode area are represented by m_B, M_B, V_M, τ, and S, respectively.[39] The CVO/CNT-rGO displays higher diffusion coefficients in the range of 1.31×10^{-9} to 1.26×10^{-11} cm^2 s^{-1} compared to CVO (9.16×10^{-10} to 1.72×10^{-12} cm^2 s^{-1}) (Fig. S12e†). Therefore, the competitive $D_{Zn^{2+}}$ of CVO/CNT-rGO could allow rapid Zn^{2+} migration, contributing to a good rate capability. According to the GITT test, the theoretical capacity of CVO/CNT-rGO is 449 mA h g^{-1} (Fig. S13†).

The electrochemical impedance spectra (EIS) of CVO, CVO/CNT, and CVO/CNT-rGO are shown in Fig. 2g, and the measurement range of the EIS test is 0.01–100 000 Hz. In the initial state, the charge transfer resistance (R_{ct}) of CVO/CNT-rGO is the smallest, and that of CVO/CNT is slightly lower compared to CVO. In addition, after 50 cycles, the R_{ct} values of the three samples are all reduced, and the CVO/CNT-rGO still shows the smallest R_{ct} compared to the other two samples. In other words, the activation (5 cycles at 0.1 A g^{-1}) process contributes to the reduction of R_{ct}. Upon the electrochemical activation process, the electrode experiences better electrolyte-infiltration and better ion diffusion is obtained, and thus the R_{ct} of the electrode is reduced.[37,38,48] At 5.0 A g^{-1}, and the initial discharge capacities of CVO, CVO@CNT, and CVO/CNT-rGO are 113, 152, and 252 mA h g^{-1}, respectively (Fig. 2h), and the corresponding capacity retention is 73%, 77%, and 87%, respectively, after 1000 cycles. CVO/CNT-rGO exhibits good cycling performance and high specific capacity, which is better than that of other reported cathode materials (Table S4†).

2.3 Mechanism of Zn^{2+} storage

The intercalation reaction mechanisms of CVO/CNT-rGO were explored by *ex situ* XRD and *ex situ* XPS (Fig. 3a). Three distinct diffraction peaks at 31.7°, 34.4°, and 35.1° appear during the discharging from 1.8 to 0.2 V, and the peak intensity gradually increases. These diffraction peaks can be regarded as layered double hydroxides $Zn_x(OTf)_y(OH)_{2x-y}\cdot nH_2O$, which is strong proof of the H^+ formation and intercalation.[49–51] H^+ is embedded in CVO/CNT-rGO during the discharging process, resulting in a local pH increase and preparation of $Zn_x(OTf)_y(OH)_{2x-y}\cdot nH_2O$. Thus, CVO/CNT-rGO in the electrolyte involves not only the intercalation of Zn^{2+} but also H^+. The (001) crystal plane at 7.0° shows the corresponding displacements and recoveries, deriving from the reversible de-embedding of H^+/Zn^{2+} during the whole charge and discharge. During the discharging to 0.2 V, the (110) crystal plane gradually shifts to a smaller angle from 25.9°, and during charging up to 1.8 V, the (110) crystal is back to its initial state, suggesting that the structural changes are reversible.[52] H^+ does not exist in the organic electrolyte, so CVO/CNT-rGO could only provide a limited specific capacity and exhibit different charge/discharge curves in the organic electrolyte. With the addition of 10 wt% H_2O into the organic electrolyte, a higher specific capacity and longer discharge plateau are observed (Fig. S14a†), which further confirms the insertion of H^+ into the CVO/CNT-rGO.[53] In addition, the CVO/CNT-rGO exhibits a faster loss of specific capacity in the organic electrolyte while better cycling stability in the aqueous electrolyte (Fig. S14b†). This suggests that crystal water may stabilize the structure during the process of electrochemical intercalation.

Ex situ XPS measurements were carried out to investigate the valence changes of the elements. The Zn signal is not detected in the initial state. During discharging to 0.2 V, the Zn 2p peaks at 1022.50 eV ($2p_{3/2}$) and 1045.58 eV ($2p_{1/2}$) are significantly enhanced due to the intercalation of Zn and precipitation of $Zn_x(OTf)_y(OH)_{2x-y}\cdot nH_2O$ (Fig. 3b). During charging to 1.8 V, the Zn signal is still detected but exhibits lower intensity, which is attributed to the partially irreversible Zn^{2+} intercalation. During discharging to 0.2 V, the intensity of V^{5+} decreases, while the intensity of V^{4+} increases, and the new peak which belongs to V^{3+} emerges. After charging back to 1.8 V, the V^{5+} and V^{4+} peaks almost completely recover to their initial state (Fig. 3c), further illustrating the highly reversible co-intercalation of Zn^{2+} and H^+. Fig. 3d shows the SEM and EDS images of the cross-section of CVO/CNT-rGO at the discharged/charged state. Zn exhibits a stronger signal in the discharged state and a weaker signal in the charged state, which is consistent with the *ex situ* XPS results (Fig. 3b) and also verifies the excellent reversible intercalation capability of the CVO/CNT-rGO. As shown in Fig. S15a and b,† the interlayer spacing at the discharged state increases from 3.46 to 3.58 Å, and therefore Zn^{2+} is probably embedded in the interlayer. In addition, the CVO/CNT-rGO electrode has a large specific surface area and is mainly controlled by capacitance (Fig. S12†), which means that some Zn^{2+} ions are adsorbed on the surface.[54,55] In other words, some of the Zn^{2+}

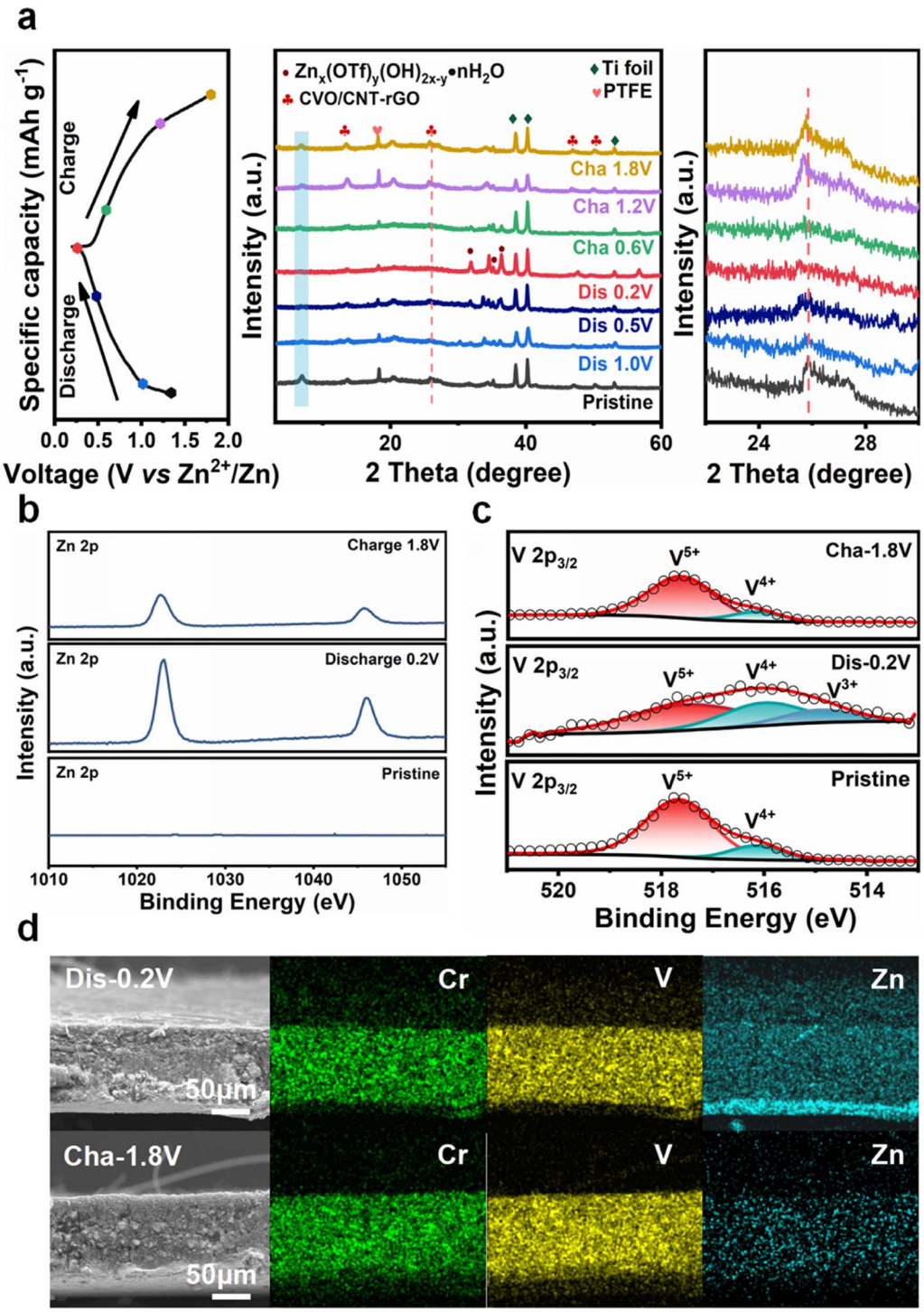

Fig. 3 (a) *Ex situ* XRD patterns of CVO/CNT-rGO during the first discharging/charging cycle. (b and c) XPS spectra of Zn 2p and V 2p during the initial discharging/charging cycle. (d) Corresponding EDS mappings at the fully discharged and charged states.

ions are embedded in the interlayer, and some are adsorbed on the surface of the material.

To further prove the prospects of CVO/CNT-rGO materials in practical applications, CVO/CNT-rGO//Zn pouch batteries with an area of 4 × 5 cm^2 and a loading of 140 mg were fabricated. Fig. 4a shows an initial discharge specific capacity of 290 mA h g^{-1} at 0.1 A g^{-1}, of which 85% is retained after 100 cycles. The GCD curves of the first five cycles of pouch cells show a stable discharge specific capacity (Fig. 4b). Fig. 4c shows that three CVO/CNT-rGO//Zn pouch cells in series still have an open-circuit voltage of 3.57 V after cycling for 100 cycles, and operate well (Fig. 4d). As shown in Fig. 4e, the cycling performance of

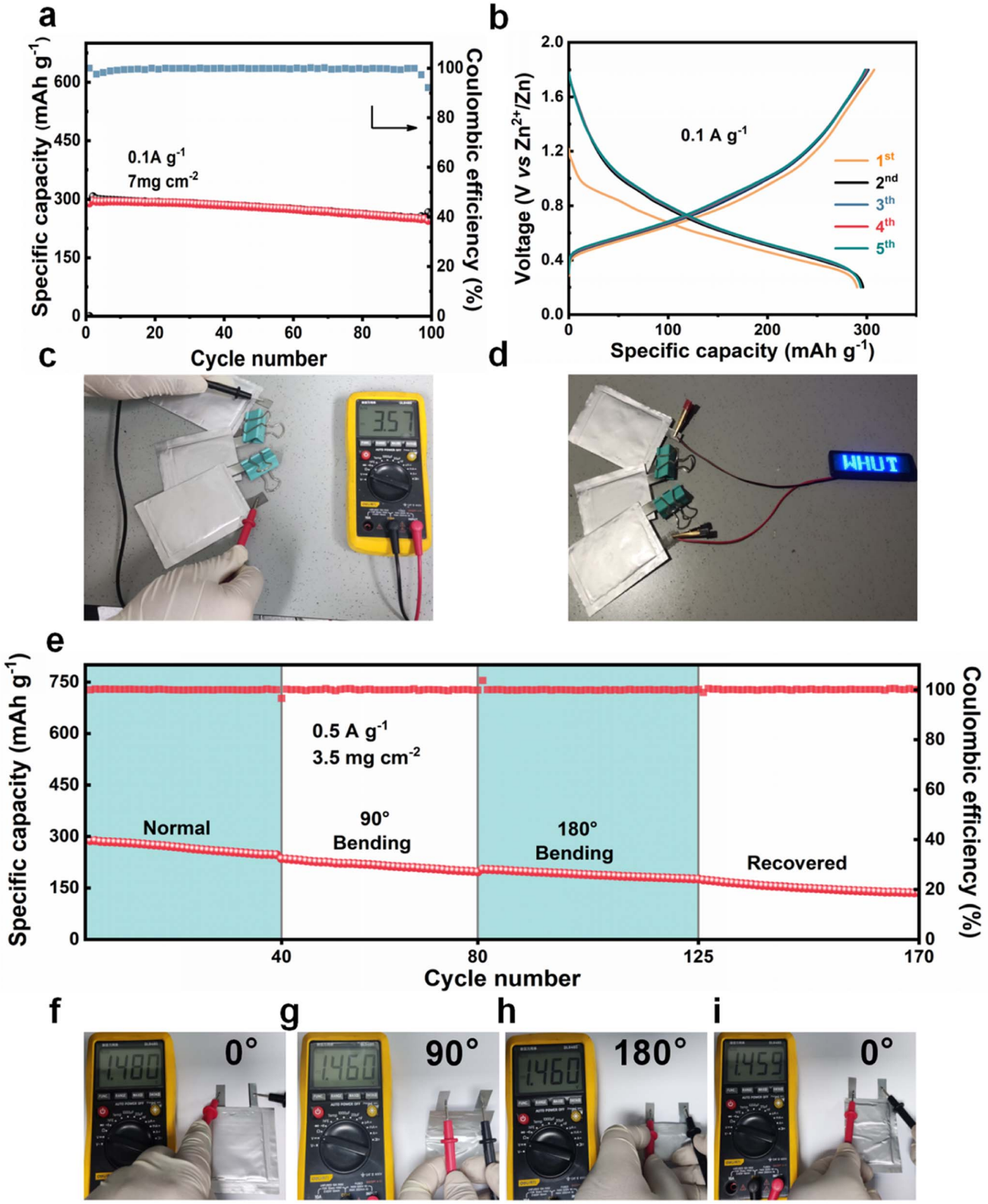

Fig. 4 (a) Cycling performance of the pouch battery at 0.1 A g^{-1}. (b) Charge and discharge curves for the first five cycles of the pouch battery. (c) The voltage of pouch batteries after 100 cycles. (d) Pouch batteries lighting up an LED sign. (e) Life testing of pouch cells at 0.5 A g^{-1} in various bending states. (f–i) The voltage of the pouch battery in different bending states.

the CVO/CNT-rGO//Zn pouch batteries was tested when bent to different angles (0°, 90°, 180°, and returned to 0°). Surprisingly, they show good flexibility and folding ability, and after 170 cycles, they still have a discharge specific capacity of 135 mA h g^{-1}. In addition, the CVO/CNT-rGO//Zn pouch batteries can maintain a stable open-circuit voltage under various bending states (Fig. 4f–i). To verify the film-forming ability of the CVO materials, independent film-forming CVO/CNT-rGO by pumping filtration was obtained (Fig. S16a†). Fig. S16b† demonstrates the bendability of this material, and Fig. S16c and d† show the SEM images of the CVO/CNT-rGO film. The above tests demonstrate the high potential of CVO/Zn pouch batteries for practical applications.

3. Conclusions

CVO/CNT-rGO composites are designed by a one-step hydrothermal method. Specifically, the induced Cr^{3+} can stabilize the lattice structure through the strong Cr–O bond, and the interconnected CNT and rGO framework can enhance the electronic conductivity and suppress the structural degradation. Moreover, CVO/CNT-rGO has a high specific capacity and reversible Zn^{2+}/H^{+} co-de-/intercalation mechanism. Consequently, high capacity (397 mA h g^{-1} at 0.2 A g^{-1}), rate capability (252 mA h g^{-1} at 5 A g^{-1}) and cyclability (87% capacity retention after 1000 cycles) are achieved for CVO/CNT-rGO cathodes. Additionally, the assembled CVO/CNT-rGO//Zn pouch cells can stably operate at different folding states. Therefore, this work designs a novel composite cathode for AZIBs, and may expands the application of AZIBs in foldable devices as well.

4. Experimental section

4.1 Synthesis of CVO/CNT-rGO

CVO, CVO/CNT, and CVO/CNT-rGO were all synthesized by simple hydrothermal methods. Firstly, NH_4VO_3 (2.66 mmol, 0.311 g) and $Cr(NO_3)_3 \cdot 9H_2O$ (1.33 mmol, 0.532 g) were dissolved in 10 mL DI water. Secondly, 0.8 g $H_2C_2O_4$ was dissolved in the above NH_4VO_3 solution. The two solutions were mixed and stirred for 1 h at room temperature. Then graphene oxide (20 mg) and multi-walled carbon nanotube slurry (20 mg) were sequentially added to the mixed solution and stirred for 0.5 h. Subsequently, the mixed solution was ultrasonicated at a low temperature for 0.5 h. The one-step hydrothermal reaction was carried out at 160 °C for 24 h. After natural cooling, the dark green powder was separated by centrifugation and lyophilized for 48 hours. The CVO/CNT-rGO powder was finally obtained.

4.2 Synthesis of CVO and CVO/CNT

For CVO, the synthesis method was similar to the above process but without the addition of graphene oxide and the multi-walled carbon nanotube slurry. The temperature was reduced to 25 °C and the powder was separated by centrifugal separation. Finally, it was dried in an oven at 70 °C overnight.

CVO/CNT was synthesized *via* a similar process to CVO/CNT-rGO, but without the addition of graphene oxide.

Author contributions

Peiqi Shi: conceptualization, data curation, investigation, methodology, writing – original draft, writing – review & editing. Meng Huang: data curation, formal analysis, project administration, writing – review & editing. Lianmeng Cui: data curation, methodology, resources. Bomian Zhang: validation, data curation, investigation. Lei Zhang: validation, project administration. Qinyou An: supervision, methodology, funding acquisition, project administration, writing – review & editing. Liqiang Mai: supervision, resources, methodology, project administration, funding acquisition, writing – review & editing.

Conflicts of interest

The authors declare no conflict of interest.

Acknowledgements

This work was supported by the National Natural Science Foundation of China (52172233), National Energy-Saving and Low-Carbon Materials Production and Application Demonstration Platform Program (TC220H06N), Hainan Provincial Joint Project of Sanya Yazhou Bay Science and Technology City (2021CXLH0007), and the Natural Science Foundation of Hubei Province (2022CFA087).

References

1 Y. Kim, Y. Park, M. Kim, J. Lee, K. J. Kim and J. W. Choi, *Nat. Commun.*, 2022, **13**, 2371.
2 J. R. Loh, J. Xue and W. S. V. Lee, *Small Methods*, 2023, **7**, 2300101.
3 P. Barnes, Y. Zuo, K. Dixon, D. Hou, S. Lee, Z. Ma, J. G. Connell, H. Zhou, C. Deng, K. Smith, E. Gabriel, Y. Liu, O. O. Maryon, P. H. Davis, H. Zhu, Y. Du, J. Qi, Z. Zhu, C. Chen, Z. Zhu, Y. Zhou, P. J. Simmonds, A. E. Briggs, D. Schwartz, S. P. Ong and H. Xiong, *Nat. Mater.*, 2022, **21**, 795–803.
4 Y. Huang, *Interdiscip. Mater.*, 2022, **1**, 323–329.
5 J. Yan, H. Huang, J. Tong, W. Li, X. Liu, H. Zhang, H. Huang and W. Zhou, *Interdiscip. Mater.*, 2022, **1**, 330–353.
6 T. Mesbahi, A. Ouari, T. Ghennam, E. M. Berkouk, N. Rizoug, N. Mesbahi and M. Meradji, *Renewable Sustainable Energy Rev.*, 2014, **40**, 204–213.
7 X. Zhang, X. Li, F. Jiang, W. Du, C. Hou, Z. Xu, L. Zhu, Z. Wang, H. Liu, W. Zhou and H. Yuan, *Dalton Trans.*, 2020, **49**, 1794–1802.
8 J. Hao, X. Li, X. Zeng, D. Li, J. Mao and Z. Guo, *Energy Environ. Sci.*, 2020, **13**, 3917–3949.
9 C. Li, S. Jin, L. A. Archer and L. F. Nazar, *Joule*, 2022, **6**, 1733–1738.
10 L. Dong, C. Xu, Y. Li, Z.-H. Huang, F. Kang, Q.-H. Yang and X. Zhao, *J. Mater. Chem. A*, 2016, **4**, 4659–4685.
11 J. Lai, H. Tang, X. Zhu and Y. Wang, *J. Mater. Chem. A*, 2019, **7**, 23140–23148.

12 Y. Li, Z. Huang, P. K. Kalambate, Y. Zhong, Z. Huang, M. Xie, Y. Shen and Y. Huang, *Nano Energy*, 2019, **60**, 752–759.
13 W. Zhang, J. Liu, W. Cai, M. Zhou, W. Zhong, G. Xiao, P. Luo, Y. Zhao and Q. An, *Chem. Eng. J.*, 2023, **464**, 142711.
14 J. Huang, J. Zeng, K. Zhu, R. Zhang and J. Liu, *Nano-Micro Lett.*, 2020, **12**, 110.
15 Q. Tan, X. Li, B. Zhang, X. Chen, Y. Tian, H. Wan, L. Zhang, L. Miao, C. Wang, Y. Gan, J. Jiang, Y. Wang and H. Wang, *Adv. Energy Mater.*, 2020, **10**, 2001050.
16 M. Huang, J. Meng, Z. Huang, X. Wang and L. Mai, *J. Mater. Chem. A*, 2020, **8**, 6631–6637.
17 G. Kasiri, J. Glenneberg, A. Bani Hashemi, R. Kun and F. La Mantia, *Energy Storage Mater.*, 2019, **19**, 360–369.
18 Z. Lin, H.-Y. Shi, L. Lin, X. Yang, W. Wu and X. Sun, *Nat. Commun.*, 2021, **12**, 4424.
19 M. Zhang, X. Zhang, Q. Dong, S. Zhang, Z. Xu, Z. Hou and Y. Qian, *Adv. Funct. Mater.*, 2023, **33**, 2213187.
20 L. Fan, Z. Li and W. Kang, *ACS Sustain. Chem. Eng.*, 2021, **9**, 5095–5104.
21 M. Du, C. Liu, F. Zhang, W. Dong, X. Zhang, Y. Sang, J. J. Wang, Y. G. Guo, H. Liu and S. Wang, *Adv. Sci.*, 2020, **7**, 2000083.
22 F. Wan, S. Huang, H. Cao and Z. Niu, *ACS Nano*, 2020, **14**, 6752–6760.
23 Y. Zhang, F. Wan, S. Huang, S. Wang, Z. Niu and J. Chen, *Nat. Commun.*, 2020, **11**, 2199.
24 J. Guan, L. Shao, L. Yu, S. Wang, X. Shi, J. Cai and Z. Sun, *Chem. Eng. J.*, 2022, **443**, 136502.
25 D. Zhang, J. Cao, Y. Yue, T. Pakornchote, T. Bovornratanaraks, J. Han, X. Zhang, J. Qin and Y. Huang, *ACS Appl. Mater. Interfaces*, 2021, **13**, 38416–38424.
26 L. Xing, C. Zhang, M. Li, P. Hu, X. Zhang, Y. Dai, X. Pan, W. Sun, S. Li, J. Xue, Q. An and L. Mai, *Energy Storage Mater.*, 2022, **52**, 291–298.
27 Y. Ran, J. Ren, Z. C. Yang, H. Zhao, Y. Wang and Y. Lei, *Small Struct.*, 2023, **4**, 2300136.
28 K. Kalaga, F. N. Sayed, M.-T. F. Rodrigues, G. Babu, H. Gullapalli and P. M. Ajayan, *J. Power Sources*, 2018, **390**, 100–107.
29 J. Zheng, C. Liu, M. Tian, X. Jia, E. P. Jahrman, G. T. Seidler, S. Zhang, Y. Liu, Y. Zhang, C. Meng and G. Cao, *Nano Energy*, 2020, **70**, 104519.
30 J. Gong, S. Yan, Y. Lang, Y. Zhang, S. Fu, J. Guo, L. Wang and G. Liang, *J. Alloys Compd.*, 2021, **859**, 157885.
31 Y. Liu, Q. Li, K. Ma, G. Yang and C. Wang, *ACS Nano*, 2019, **13**, 12081–12089.
32 P. He, J. Liu, X. Zhao, Z. Ding, P. Gao and L.-Z. Fan, *J. Mater. Chem. A*, 2020, **8**, 10370–10376.
33 D. Chao, C. Zhu, M. Song, P. Liang, X. Zhang, N. H. Tiep, H. Zhao, J. Wang, R. Wang, H. Zhang and H. J. Fan, *Adv. Mater.*, 2018, **30**, 1803181.
34 Z. Liu, D. Wang, Z. Tang, G. Liang, Q. Yang, H. Li, L. Ma, F. Mo and C. Zhi, *Energy Storage Mater.*, 2019, **23**, 636–645.
35 S. Wang, Q. Wang, W. Zeng, M. Wang, L. Ruan and Y. Ma, *Nano-Micro Lett.*, 2019, **11**, 70.
36 H. Liu, N. Wang, L. Hu, M. Sun, Z. Li and C. Jia, *Electrochim. Acta*, 2023, **441**, 141856.
37 J. Xu, Y. Zhang, C. Liu, H. Cheng, X. Cai, D. Jia and H. Lin, *Small*, 2022, **18**, 2204180.
38 Z. Feng, Y. Zhang, X. Yu, Y. Yu, C. Huang and C. Meng, *Colloids Surf., A*, 2022, **641**, 128473.
39 J. Wang, J. Wang, Y. Jiang, F. Xiong, S. Tan, F. Qiao, J. Chen, Q. An and L. Mai, *Adv. Funct. Mater.*, 2022, **32**, 2113030.
40 Y. Hai, K. Tao, H. Dan, L. Liu and Y. Gong, *J. Alloys Compd.*, 2020, **835**, 155254.
41 C. Liu, Z. Neale, J. Zheng, X. Jia, J. Huang, M. Yan, M. Tian, M. Wang, J. Yang and G. Cao, *Energy Environ. Sci.*, 2019, **12**, 2273–2285.
42 K. Zhu, S. Wei, H. Shou, F. Shen, S. Chen, P. Zhang, C. Wang, Y. Cao, X. Guo, M. Luo, H. Zhang, B. Ye, X. Wu, L. He and L. Song, *Nat. Commun.*, 2021, **12**, 6878.
43 X. Ma, X. Cao, M. Yao, L. Shan, X. Shi, G. Fang, A. Pan, B. Lu, J. Zhou and S. Liang, *Adv. Mater.*, 2021, **34**, 2105452.
44 Z. Pang, B. Ding, J. Wang, Y. Wang, L. Xu, L. Zhou, X. Jiang, X. Yan, J. P. Hill, L. Yu and Y. Yamauchi, *Chem. Eng. J.*, 2022, **446**, 136861.
45 N. Liu, X. Wu, L. Fan, S. Gong, Z. Guo, A. Chen, C. Zhao, Y. Mao, N. Zhang and K. Sun, *Adv. Mater.*, 2020, **32**, 1908420.
46 H. Chen, J. Huang, S. Tian, L. Liu, T. Qin, L. Song, Y. Liu, Y. Zhang, X. Wu, S. Lei and S. Peng, *Adv. Sci.*, 2021, **8**, 2004924.
47 Y. Du, X. Wang, Y. Zhang, H. Zhang, J. Man, K. Liu and J. Sun, *Chem. Eng. J.*, 2022, **434**, 134642.
48 Q. Zong, Y. Zhuang, C. Liu, Q. Kang, Y. Wu, J. Zhang, J. Wang, D. Tao, Q. Zhang and G. Cao, *Adv. Energy Mater.*, 2023, **13**, 2301480.
49 H. Huang, X. Xia, J. Yun, C. Huang, D. Li, B. Chen, Z. Yang and W. Zhang, *Energy Storage Mater.*, 2022, **52**, 473–484.
50 Q. Zhao, Y. Zhu, S. Liu, Y. Liu, T. He, X. Jiang, X. Yang, K. Feng and J. Hu, *ACS Appl. Mater. Interfaces*, 2022, **14**, 32066–32074.
51 B. Sambandam, S. Kim, D. T. Pham, V. Mathew, J. Lee, S. Lee, V. Soundharrajan, S. Kim, M. H. Alfaruqi, J.-Y. Hwang and J. Kim, *Energy Storage Mater.*, 2021, **35**, 47–61.
52 G. Xu, X. Liu, S. Huang, L. Li, X. Wei, J. Cao, L. Yang and P. K. Chu, *ACS Appl. Mater. Interfaces*, 2019, **12**, 706–716.
53 K.-W. H. Lulu Wang, J. Chen and J. Zheng, *Sci. Adv.*, 2019, **5**, eaax4279.
54 Y. Jiang, H. Xu, L. Ren, M. Ji, X. Shen and S. Li, *Energy Fuels*, 2021, **35**, 17948–17955.
55 X. Zhu, Z. Cao, X.-L. Li, L. Pei, J. Jones, Y.-N. Zhou, P. Dong, L. Wang, M. Ye and J. Shen, *Energy Storage Mater.*, 2022, **45**, 568–577.

